NANO LETTERS

pubs.acs.org/NanoLett

Letter

# Unclonable Three-Level Holograms for Two-Factor Visual Authentication via One-Step Cascade-Nanostructure Imprinting

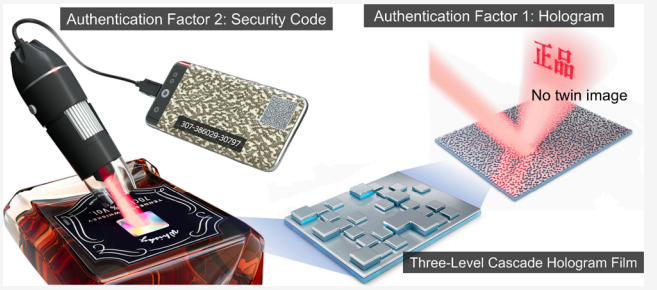
Jinhyeok Yang, Myeonggyu Choi, Ji-Hwan Ha, Jihyeon Ahn, Soon Hyoung Hwang, Sohee Jeon, Dabin Kim, Jaehoon Jeong, Minki Kim, Hakhyun Lim, Byung-Ho Kang, Jong-An Choi, Byeongmin Kang, Hwi Kim,* Junseong Ahn,* and Jun-Ho Jeong*

Cite This: *Nano Lett.* 2026, 26, 9836−9846

Read Online

ACCESS | Metrics & More | Article Recommendations | Supporting Information

**ABSTRACT:** Digital authentication technologies are increasingly threatened by the rapid advance of artificial intelligence and sophisticated cyberattacks. Against this backdrop, analog approaches that enable intuitive visual inspection and are physically unclonable are gaining prominence. This work develops a low-cost route to fabricate large-area hologram films with cascade nanostructures, establishing a robust two-factor authentication platform. Three-level silicon master molds are produced in a single dry-etching step, and the hologram films are replicated via nanoimprint lithography. By integrating a computer-generated holography design, the holograms selectively suppress the conjugate image, enabling instant visual authentication using a portable flashlight. To strengthen security, each film incorporates fiducial marks that designate the inspection site for a portable microscope. The local nanopattern can be converted into a security code for secondary verification. Consequently, the proposed cascade-hologram strategy combines cost-effectiveness, high fidelity, and durability with enhanced anticounterfeiting performance, supporting deployment across products, including electronic devices, apparel, and consumer goods.



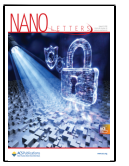

**KEYWORDS:** *Two-factor authentication, Three-level cascade nanostructure, Diffractive optical elements (DOEs), Nanoimprint lithography (NIL), Microloading effect*

Security identification and authentication technologies have become increasingly critical, finding extensive applications in diverse fields including financial transactions, data management, and protection of valuable physical assets.[1,2] These technologies are broadly classified into digital and analog approaches. Digital identification and authentication technologies, such as near field communication (NFC) and quick response (QR) codes, have been widely adopted due to their convenience, rapid data processing capabilities, and ease of integration into mobile payments and user authentication systems.[3−7] However, despite these advantages, digital methods remain vulnerable to security threats including hacking, phishing attacks, and malicious redirection, and these risks are further exacerbated by rapidly advancing artificial intelligence and increasingly sophisticated cyberattacks.[8−10]

Consequently, analog security methods such as holograms, watermarks, and security threads continue to play a pivotal role in authenticating and securing valuable physical items, such as currency, artworks, and pharmaceuticals.[11−14] Analog technologies offer robust, durable, and inherently replication-resistant verification features, making them substantially more resilient to advanced counterfeiting techniques compared to digital counterparts.[15−17] Among these analog approaches, diffractive optical elements (DOEs), particularly holograms, have attracted significant attention due to their unique optical properties, visual distinctiveness, and intuitive authentication processes, thereby enhancing consumer trust and safeguarding brand integrity.[18−21]

Therefore, researchers have explored various configurations of DOEs, each characterized by specific advantages and limitations. Binary DOEs, for instance, are cost-effective and relatively simple to fabricate, yet their limited diffraction efficiency often results in issues such as twin images, speckle noise, and reduced image resolution.[22−24] On the other hand, multilevel DOEs achieve superior diffraction efficiency but typically require complex and costly fabrication techniques.[25−27] High-resolution lithographic methods, including electron-beam lithography and multiphoton lithography, deliver precise

**Received:** April 22, 2026
**Revised:** June 1, 2026
**Accepted:** June 3, 2026
**Published:** June 18, 2026



Downloaded from pubs.acs.org/naleif/article-pdf/26/30/9836/6514034/acs.nanolett.6c01958.pdf by KOREA UNIV user on 14 August 2026

ACS Publications

© 2026 American Chemical Society



https://doi.org/10.1021/acs.nanolett.6c01958
*Nano Lett.* 2026, 26, 9836−9846

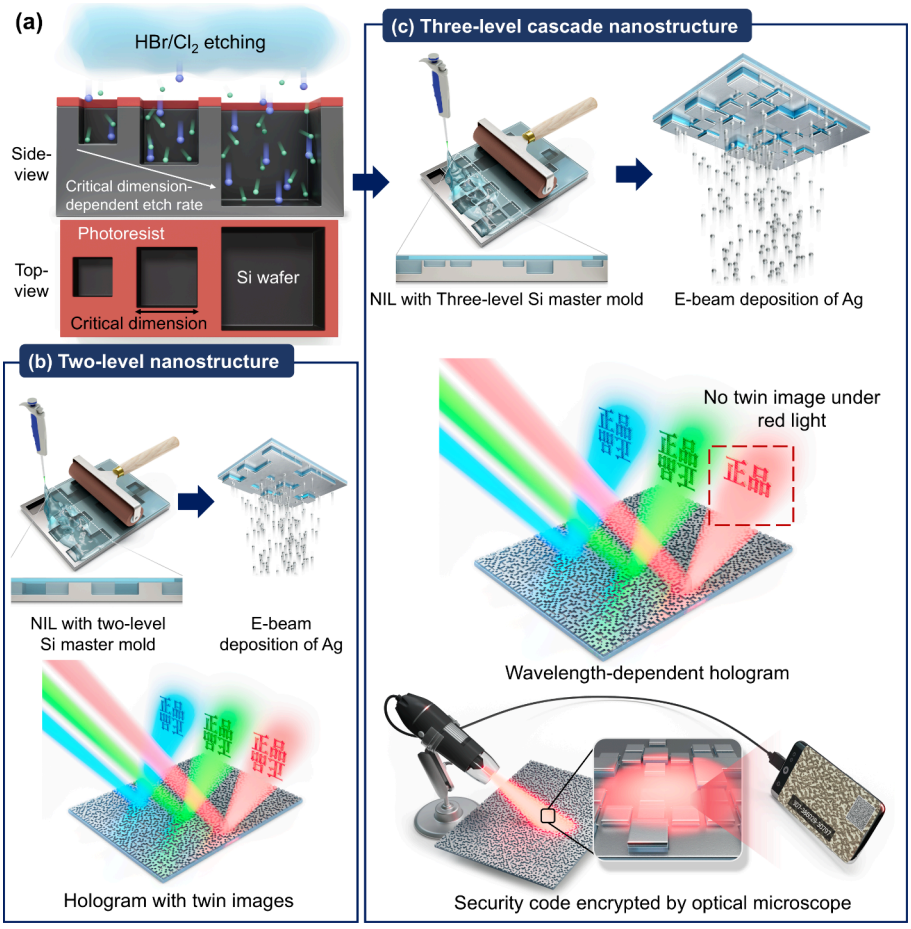



**Figure 1.** Schematic illustration of a nanostructure-enabled, two-factor holographic security platform. (a) Process strategy for fabricating a three-level silicon (Si) master mold by exploiting the microloading effect during $HBr/Cl_2$ reactive-ion etching (RIE). When the critical dimension (CD) is narrow, the local etch rate decreases, producing a shallower relief; conversely, wider CDs experience faster etching and thus yield deeper features. (b) Reference two-level hologram film. A conventional two-level Si master mold replicated in a single NIL step produces a binary hologram film, which inevitably shows twin images under illumination at every wavelength. (c) Concept and security application of the three-level hologram film. A cascade nanostructure is first defined on a Si wafer through krypton fluoride (KrF) lithography followed by $HBr/Cl_2$ RIE. The Si master mold is then replicated into a polymer stamp via NIL, and an Ag coating is deposited to complete the hologram film. The final film suppresses conjugate image at a designated wavelength (e.g., red light) while incorporating a nanoscale pattern readable only under portable microscope, thereby delivering two independent security factors.

nanopatterning but remain economically unfeasible for large-scale manufacturing.[28] Thus, for practical and reliable implementation of analog security systems, the development of cost-effective, scalable, and large-area fabrication techniques suitable for multilevel DOEs is crucial.

In parallel, despite ongoing technological advancements, various counterfeiting methods have unfortunately emerged, attempting to replicate only the visual features of holograms without accurately reproducing their intricate nanopattern structures.[29] Such superficial imitations undermine consumer confidence and diminish the effectiveness of conventional holographic authentication. Therefore, there is an urgent need to develop more sophisticated analog authentication systems that leverage the intrinsic complexity and irreproducibility of holographic nanopatterns.

Herein, we propose a large-area nanoimprinted cascade nanostructure for two-factor authentication, aiming to address the critical need for advanced analog security systems. Specifically, the proposed security pattern leverages three-level cascade nanopatterns to provide two distinct authentication mechanisms. One is easily verifiable visual authentication through holographic imaging, and the other is secondary verification via intricate internal nanopattern features discernible only under microscopic examination, as shown in Figure 1. To realize this two-factor authentication approach, the developed system encompasses four main strategies: (1) a synergistic combination of nanoimprint lithography (NIL) with microloading effects-based anisotropic reactive-ion etching (RIE), enabling scalable and cost-effective fabrication of large-area three-level cascade nanostructures; (2) a rational hologram design based on computer-generated holography (CGH), optimizing three-level structures to exclusively eliminate twin (conjugate) images at the red wavelength; (3) incorporation of nanopattern dimensions at the minimal scale observable by optical microscopy, enabling embedded security codes within the nanopatterns for enhanced verification; and (4) demonstration of practical applicability and versatility by successfully integrating the developed two-factor authentication system onto diverse physical items, including technical equipment, luxury apparel, and high-value consumer goods such as whiskey bottles. The developed approach offers significant promise for enhancing security standards in authentication technology,

Downloaded from pubs.acs.org/nalefd/article-pdf/26/30/9836/6514034/acs.nanolett.6c01958.pdf by KOREA UNIV user on 14 August 2026


https://doi.org/10.1021/acs.nanolett.6c01958
Nano Lett. 2026, 26, 9836−9846

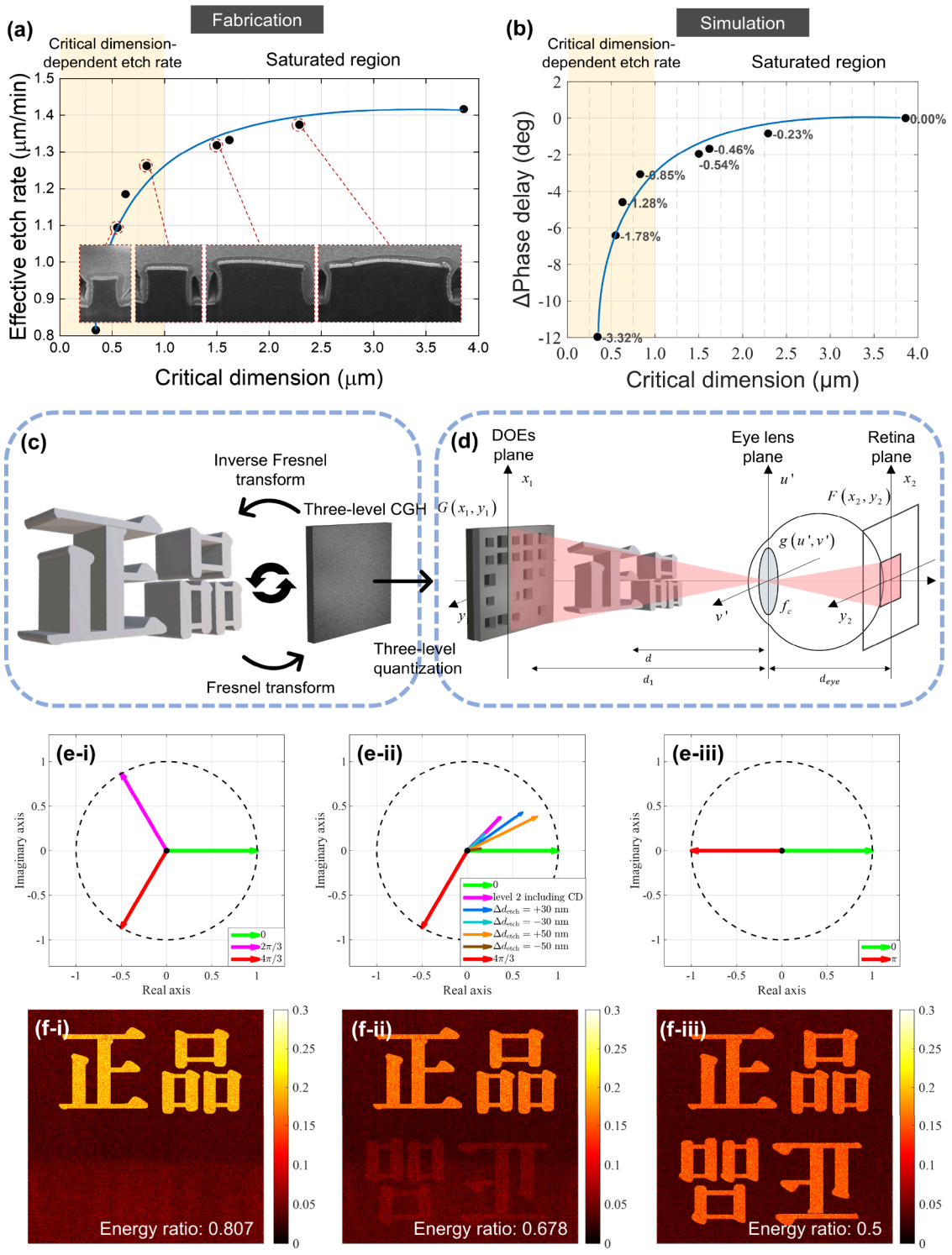



**Figure 2.** Hologram design and simulation. (a) Effective etch rate as a function of critical dimension and cross-sectional image of hologram film. (b) Effective phase deviation and relative errors as a function of CD. (c) Schematic illustration of iterative Fresnel transform algorithm. (d) Schematic illustration of CdFrt-based observation simulation (see details in Figure S1). (e) Phase modulation for three-type DOEs. (e-i) ideal three-level DOEs; (e-ii) three-level DOEs with CD. When only the CD effect is considered, the level 2 pixel exhibits a phase delay of 46.12°. Under fabrication tolerances, the phase delays of the level 2 pixel induced by $\Delta d_{etch}$ are −10.76° and −0.92° for $\Delta d_{etch} = \pm 30$ nm, respectively, and −19.61° and −37.11° for $\Delta d_{etch} = \pm 50$ nm, respectively. Furthermore, the pixel intensity is 0.52 when only the CD effect is considered, whereas the intensity of the level 2 pixel varies to 0.74 and 0.26 for $\Delta d_{etch} = \pm 30$ nm, respectively, and to 0.86 and 0.15 for $\Delta d_{etch} = \pm 50$ nm, respectively (see details in Figure S2 and Figure S3); (e-iii) binary-level DOEs. (f) Reconstructed 正品 images for three-type DOEs and the energy ratio between the primary and twin images (see details in Figure S4). (f-i) ideal three-level DOEs; (f-ii) three-level DOEs with CD; (f-iii) binary-level DOEs.



https://doi.org/10.1021/acs.nanolett.6c01958
Nano Lett. 2026, 26, 9836−9846

Downloaded from pubs.acs.org/nalefd/article-pdf/26/30/9836/6514034/acs.nanolett.6c01958.pdf by KOREA UNIV user on 14 August 2026

providing robust protection against increasingly sophisticated counterfeiting threats and establishing a valuable foundation for future research and commercial applications.

## HOLOGRAM DESIGN AND SIMULATION

In the practical DOE (hologram film) fabrication process proposed in this study, a three-level silicon (Si) master mold for NIL is fabricated in a single RIE process by exploiting the microloading effect. Furthermore, in the design of three-level DOEs, accurate three-level phase modulation ($0,2\pi/3,4\pi/3$) are important to ensure proper pixel functionality and to suppress twin image. Therefore, prior to designing a photomask with a three-level nanostructured diffraction pattern, the etch rate was analyzed as a function of the critical dimension (CD), as shown in Figure 2a, to obtain accurate information on depth formation. The microloading effect is a phenomenon whereby the etch rate depends on the nanopattern width; within a certain CD range, narrower CDs are etched more shallowly, whereas wider CDs are etched more deeply.[30,31] For narrow CDs ($\leq 1$ $\mu$m; highlighted region on the left side of the graph), access of reactive species is hindered and byproducts of the etching reaction adsorb onto or clog the sidewalls, suppressing the plasma reaction and rendering the etch rate CD-dependent. However, the etch depth does not increase dependently with increasing CD; beyond a specific CD ($\geq 1$ $\mu$m; saturated region on the right side of the graph), access of reactive species and removal of byproducts proceed smoothly, and the etch rates become similar. On the basis of this information, by appropriately discretizing the feature sizes in the photomask during design, a Si master mold with discretized depths can be fabricated through dry etching. Furthermore, to evaluate the etch-rate-induced phase modulation, the effective phase deviation of a single DOE pixel was simulated as a function of the effective etch rate. Using a CD of 4 $\mu$m as the reference, Figure 2b shows the effective phase deviation and the relative errors in phase delay as a function of CD.

In the reflective DOEs designed for this study, the pixels at each level are intended to modulate phase delays of 0, $2\pi/3$, and $4\pi/3$, respectively. As described in Figure 2a, the pixels responsible for 0 and $4\pi/3$ phase delays are not significantly affected by the CD. However, for the level 2 pixels designed to achieve a $2\pi/3$ phase delay, the effective phase-modulating region increases with pixel height due to the influence of the CD. The actual phase delay induced by each level 2 pixel is thus determined by vectorially averaging the contributions of the modulating and nonmodulating regions into a single equivalent phase vector per pixel. To accurately reflect this behavior, the effective phase-active regions of the level 2 pixels were taken into account when determining the actual phase values. Based on the analysis shown in Figure 2 and eq 1, the etch depths were set to 830 nm for level 2 and 930 nm for level 3, ensuring the intended phase modulation while maintaining fabricability.

To generate ideal phase-only CGH suitable for reflective three-level DOEs, we adopted a modified synthesis approach. While conventional iterative Fourier transform algorithms (IFTA) generate phase-only CGH by modeling the relationship between the hologram and image planes using fast Fourier transform (FFT) and inverse FFT, our method employs the Fresnel transform instead, as illustrated in Figure 2c. This allows the virtual image reconstructed from the phase-only CGH to appear at a finite propagation distance rather than in the far field, which is a key advantage of our approach. Regarding this iterative synthesis process, we did not modify the target phase map to precompensate for fabrication tolerances during the design stage. Instead, we adopted a strategy of directly incorporating realistic physical constraints into the simulation to verify the robustness of our three-level design. Specifically, the iterative Fresnel transform was first performed to generate a continuous phase-only CGH by iteratively enforcing intensity constraints in the image plane. To produce a three-level phase pattern compatible with the fabricated reflective DOEs, the resulting continuous phase was then quantized into three discrete levels, which ultimately determines the CD of the pixels. Finally, the CD-dependent phase degradation effect, as analyzed in Figure 2b, was explicitly incorporated into the forward simulation of the quantized CGH to evaluate the realistic reconstruction performance. This approach allows for a more rigorous assessment of how the device performs under actual fabrication constraints. The phase delay induced by the reflective DOE is given by the equation

$$\Delta\phi = \frac{2\pi}{\lambda}(n_{air} \times 2d_{etch}) + \pi \tag{1}$$

where $n_{air}$ is the refractive index of air, $d_{etch}$ represents the physical etch depth, and $\lambda$ denotes the wavelength, which is set to 632 nm. Additionally, $\pi$ phase shift is introduced due to reflection at the interface between air and Ag. To observe the virtual image formed at a finite distance by the synthesized three-level DOEs, we employed a cascaded Fresnel transform (CdFrt)-based eye model,[32] as illustrated in Figure 2d. In this model, $d_{eye}$ denotes distance from the eye lens to the DOEs plane, $d_{retina}$ represents distance from the retina plane to the eye lens plane, and $d_f$ is distance from the focal plane to the eye lens plane. $f_{eye} = (d_f d_{eye})/(d_f + d_{eye})$ is focal length of eye. $\rho$ is radius of eye. In our simulations, both $d_{ey}$ and $d_f$ were set to 20 cm, while $d_{retina}$ was fixed at 25 mm and $\rho$ was fixed at 3 mm. The optical fields are denoted by $D(x_1,y_1)$ at the DOEs plane, at the eye lens plane by $E(u,v)$, and at the retina plane by $R(x_2,y_2)$. Figure 2e-i illustrates the ideal complex modulation behavior of individual pixels in three-level DOEs. Figure 2e-ii shows the phase and amplitude modulation behavior of the three-level DOEs when CD is taken into account. Figure 2e-iii shows the phase modulation behavior of the binary-level DOEs. Figure 2f-i shows the simulated observation result of the ideal three-level DOEs, unaffected by the CD, using the CdFrt based eye model. In this case, the twin image is successfully suppressed, and the intensity of the original image is enhanced, both of which represent the main objectives of three-level encoding. Figure 2f-ii presents the observation results of three-level DOEs considering the effects of the critical dimension. Since the level 2 pixels cannot modulate a full $2\pi/3$ phase delay, the twin image is not entirely suppressed compared to the ideal case, and the intensity of the original image is slightly enhanced. For comparison, Figure 2f-iii presents the observation result of conventional binary-level DOEs, where the twin image can be clearly observed with the same energy as the original image, thereby highlighting the limitation of binary-level design and underscoring the necessity of adopting a three-level design.

The Chinese character phrase 正品 designed in this study has long been used in East Asia to signify "genuine or authentic goods," and was selected as it is deemed suitable for simple primary visual authentication.

Downloaded from pubs.acs.org/naleif/article-pdf/26/30/9836/6514034/acs.nanolett.6c01958.pdf by KOREA UNIV user on 14 August 2026



https://doi.org/10.1021/acs.nanolett.6c01958
Nano Lett. 2026, 26, 9836−9846

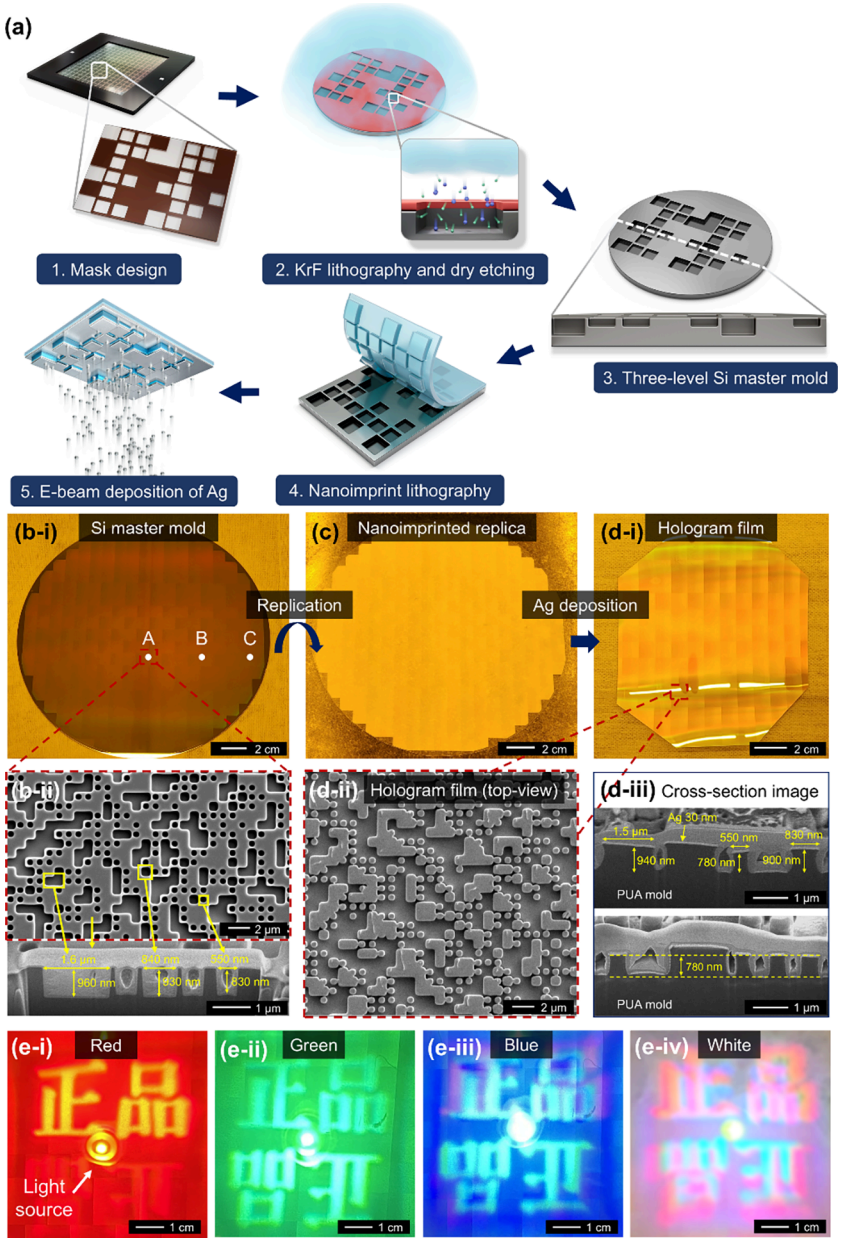



**Figure 3.** Fabrication process and structural characterization of the cascade hologram via SEM/FIB analysis. (a) Stepwise process flow for large-area three-level hologram fabrication. Patterns are defined on photoresist (PR) by KrF lithography after photomask design, followed by dry-etching to create a three-level Si master mold. The nanostructure is then replicated into a polymer mold by NIL, and finally Ag is deposited onto the polymer replica by electron-beam evaporation to complete the hologram film. (b) Structural analysis of the three-level Si master mold. (b-i) top-view schematic of the Si master mold; (b-ii) SEM top-view and cross-sectional view images. (c) PUA polymer mold replicated via NIL. (d) Structural analysis of the completed Ag-coated hologram film. (d-i) top-view image of the large-area hologram film; (d-ii) SEM top-view image; (d-iii) SEM cross-sectional view image. (e) Comparison of hologram reconstructions under different illumination wavelengths. (e-i) red light (632 nm), (e-ii) green light (532 nm), (e-iii) blue light (365 nm), and (e-iv) white light (broadband emission).

## THREE-LEVEL CASCADED HOLOGRAM FILMS FABRICATION AND VALIDATION

The fabrication process for the three-level Si master mold and the corresponding large-area hologram film developed in this study is schematically illustrated in Figure 3a, while a detailed comparison with the two-level process can be found in Figure S5. The mask pattern designed by CGH (Figure 3a-1) is transferred onto a photoresist (PR) layer spin coated on a Si wafer by krypton fluoride (KrF) lithography, after which the exposed PR is removed during development. Anisotropic dry-etching (Figure 3a-2) follows; due to the microloading effect, narrower trenches experience a reduced etch rate and consequently attain shallower depths than wider ones, thereby forming a three-level relief on the Si wafer (Figure 3a-3). The resulting Si master mold is replicated via NIL using a ultraviolet (UV)-curable resin to yield an inverse polymer mold (Figure 3a-4), onto which a 30 nm thick Ag layer is deposited by electron beam evaporation (Figure 3a-5), thereby enhancing reflectivity and diffraction efficiency.

Figure 3b-I presents a photograph of the Si master mold fabricated by KrF lithography, and Figure 3b-ii displays top view and cross-sectional scanning electron microscope (SEM)/focused ion beam (FIB)-SEM images of its nanopatterns.

Downloaded from pubs.acs.org/nalefd/article-pdf/26/30/9836/6514034/acs.nanolett.6c01958.pdf by KOREA UNIV user on 14 August 2026


https://doi.org/10.1021/acs.nanolett.6c01958
Nano Lett. 2026, 26, 9836−9846




**Figure 4.** Two-factor security application of the developed hologram film. (a) Concept of two-factor authentication. Primary hologram image authentication using a portable flashlight (left) and secondary encrypted nanopattern verification using a portable microscope (right). (b) Authentication via the hologram image. When the hologram film is illuminated by a portable flashlight, a predefined holographic image appears visible to the naked eye. Each hologram film carries a fiducial mark that enables secondary authentication. (c) Microscopic security code authentication. (c-i) Nanomicro scale diffraction pattern readable by portable optical microscope. (c-ii) Image processing step that isolates individual objects by separating pixels and connected pattern features. (c-iii) Extraction of security code elements from the processed image, including the number of isolated areas, pixel count as a measure of size, and fill ratio. Security code is uniquely generated, preventing replication without the identical nanofabrication process. (c-iv) Average values of the security code elements obtained from five different films.

Downloaded from pubs.acs.org/nalefd/article-pdf/26/30/9836/6514034/acs.nanolett.6c01958.pdf by KOREA UNIV user on 14 August 2026



https://doi.org/10.1021/acs.nanolett.6c01958
Nano Lett. 2026, 26, 9836−9846

Cross sectional measurements reveal etch depths of 830 nm for 550 nm wide pixels, 930 nm for 840 nm pixels, and 960 nm for features wider than the CD (e.g., 1.6 $\mu$m). Additionally, the etch depth of the 550 nm-wide features was measured at the three locations marked A, B, and C in Figure 3b-i. The average depth was 828.71 nm, with a standard deviation of 4.65 nm (Figure S6). These results indicate that uniform etch depths can be achieved across the entire master mold through a single dry-etching process, regardless of whether the patterned region is located near the center or the edge of the mold. The NIL replicated polymer film is shown in Figure 3c, and the completed Ag coated hologram film in Figure 3(d-i). A top view image (Figure 3d-ii) confirms faithful inversion of the master pattern, and the diverse diffraction motifs observed at different positions indicate their potential as unique authentication cues. The cross sectional FIB-SEM in Figure 3(d-iii) indicates that volume shrinkage of the polymer during UV curing reduces the feature heights relative to the master mold.[33] The etch depth of the 550 nm pixels (level 2) decreased from 830 to 780 nm, corresponding to a 50 nm reduction, whereas the 840 nm pixels (level 3) contracted from 930 to 900 nm, a 30 nm decrease. Features with CDs larger than 840 nm attained a maximum depth of roughly 940 nm, exhibiting only a marginal difference from level 3. This behavior deviates from that expected under an ideal uniform volumetric shrinkage model, in which wider features would generally undergo greater height reduction than narrower ones.[34] However, the replicated topography can be affected by compressive stresses at the sidewalls and top surface of the master mold, the residual layer thickness of the resist, the spatial distribution of UV irradiation, and deformation during demolding.[35−37] These process-dependent factors may account for the observed nonuniform height reduction. Because such deviations can reduce the fidelity of the holographic image, additional simulation-based validation was performed. Although the reconstructed image quality was lower than that obtained under the ideal height condition, the twin image was still effectively suppressed. (The simulation-based validation is shown in Figure S7.) The lower cross section in Figure 3d-iii demonstrates a uniform height of 780 nm for all 550 nm pixels, attesting to the high uniformity of the hologram film. Additionally, five different hologram films were replicated from the same master mold, and their cross-sectional profiles were examined by FIB-SEM analysis. The results confirmed the high reproducibility of the NIL replication process (Figure S8). In the present layout, three discrete relief tiers are defined, namely an unpatterned area (level 1), 780 nm deep features (level 2), and features ≥900 nm deep (level 3). As shown in Figure 2a, during dry-etching, features with line widths ≤1 $\mu$m exhibit line width-dependent etch rates, thereby generating multiple etch depths. Therefore, for features with line widths ≤1 $\mu$m, further partitioning of the CDs along with a carefully engineered three-level photomask could yield Si master molds with a greater number of relief levels and, in turn, hologram films with a more finely graded cascade profile. For line widths above 1 $\mu$m, however, the microloading effect is still significantly reduced, and the etch depth converges such that no additional height difference is observed. Although the cascade heights measured in the replicated film deviate slightly from the nominal design values, these discrepancies are expected to be substantially mitigated by precompensating for volume shrinkage during the master mold design process or by using a resist with minimal polymerization shrinkage.[38,39]

Figure 3e verifies that the fabricated film does not generate a conjugate image of the 正品 hologram under red illumination (Figure 3e-i), whereas prominent twin images appear under green (Figure 3e-ii) and blue light (Figure 3e-iii)). Figure 3e-iv displays a photograph of the hologram irradiated with the white light flash from a smartphone. By design, the film suppresses the conjugate image exclusively in the red spectral band while still generating twin images at all other wavelengths. Consequently, under broadband illumination the lower portion of the hologram emits light devoid of its red component, producing the characteristic cyan hue arising from the additive mixing of green and blue (Figure S9). Figure S10a shows the RGB intensity maps extracted under each illumination condition. Under white-light illumination, unlike the other cases, the red-channel intensity is selectively suppressed in the conjugate-image region, appearing dark owing to its low intensity, whereas the green and blue channels remain visible. This result supports the formation of the cyan conjugate image. In addition, Figure S10b presents RGB edge maps showing the spatial distribution of each color component, further confirming the wavelength-selective suppression of the red component in the conjugate image.

Finally, to assess the practical applicability of the hologram film under real-world use conditions, a single hologram film was sequentially subjected to five durability tests, including high-temperature exposure, low-temperature exposure, washing, bending, and abrasion tests (Figure S11).[40] Although the film exhibited noticeable degradation under repeated sandpaper abrasion, this limitation is expected to be mitigated in future implementations by introducing an additional protective overlayer.

In summary, the wavelength-selective absence of the twin image under practical use conditions can be exploited as a primary authentication cue using a commercial flashlight, and, when necessary, the same verification can be performed simply with a smartphone flashlight.

## TWO-FACTOR AUTHENTICATION APPLICATION AND MECHANISM

Figure 3 shows that the hologram film contains finely engineered nanopatterns and blocks the conjugate image in a wavelength dependent way, a property that can be exploited for security and authentication. Figure 4a outlines representative uses. When the film is attached to a valuable item, a twin image appears under every illumination wavelength except the design specified one (red light in this study). A simple visual check of the twin image therefore provides primary authentication. To strengthen protection and curb counterfeiting, a predefined spot whose location is known only to the authorized user is selected for secondary authentication. The diffraction pattern at this spot is captured with a portable microscope and converted into a numeric security code.

Figure 4b presents photographs of three products carrying the film. For each label, red light was used to test twin image suppression. The image above the light source remains bright, whereas the conjugate image below is almost invisible. Each film also bears a fiducial mark (equipment 1, bottle 2, apparel 3) that specifies where to collect the nano pattern for the security code; red circles on the bottle and apparel mark these spots. In other words, the region designated for portable microscope interrogation varies from one intricately patterned hologram film to another, thereby guaranteeing a markedly higher level of security. Using a commercial hand-held microscope with a

Downloaded from pubs.acs.org/naleif/article-pdf/26/30/9836/6514034/acs.nanolett.6c01958.pdf by KOREA UNIV user on 14 August 2026



https://doi.org/10.1021/acs.nanolett.6c01958
Nano Lett. 2026, 26, 9836−9846

maximum magnification of 1600×, nanostructures as small as ~500 nm can be resolved. Consequently, the hologram film was engineered with a minimum line width of 550 nm, enabling its entire nanopattern to be clearly visualized under the portable microscope at its highest magnification. The encoding procedure for the bottle label appears in Figure 4c. An optical micrograph of the chosen region (Figure 4c-i) reveals bright raised zones and dark recessed zones. After binarization, the raised areas are isolated, producing the segmented map in Figure 4c-ii (details in Figure S12). From this map, three parameters, namely the number of isolated areas, average size, and fill ratio, are extracted and combined into a serial number. To examine the statistical distribution of security-code parameters generated from different local nanopatterns, one randomly selected region from each of five hologram films replicated from the same Si master mold was analyzed (Figure S13; the bottle label corresponds to Sample 1). The number of isolated areas, average size, and fill ratio were 326 ± 14.60, 366 ± 18.00, and 31 ± 0.39%, respectively (Figure 4c-iii). Additional analyses were performed at the same fiducial position under varied imaging conditions, including different focal positions and combined variations in microscope illumination intensity (Figure S14). When only the focal position was changed, slight deviations were observed in the extracted parameters. In contrast, changes in illumination intensity had a strong influence on the generated security code, as detailed in Figure S15. This dependence can introduce significant errors during security-code generation. In future work, this limitation could be mitigated by incorporating deep-learning-based image processing for more precise edge detection and area segmentation. Importantly, this practical requirement for standardized readout does not compromise the uniqueness of the security code. Because the nanopattern varies continuously across the entire film, shifting the observation window by only a few micrometres yields an entirely different security code. The fiducial mark therefore both designates the exact region to be imaged with a portable microscope and provides a platform for generating virtually unlimited, non-overlapping security codes. Although the present platform is not completely immune to all possible attacks, such as theft of the Si master mold or complete reverse engineering of the nanostructure enabled by advanced technologies, its significance lies in demonstrating practical anticounterfeiting capability.

In summary, the CGH based three-level hologram film allows rapid primary authentication through wavelength selective twin image suppression and adds robust secondary verification via unique, microscope readable diffraction codes. Together these features offer a strong barrier against counterfeiting.

In conclusion, this study establishes a fabrication route for three-level Si master molds by exploiting the area-dependent etch rate achievable within a single dry-etching step. On the basis of these molds, large-area cascade-nanostructured holographic films were efficiently replicated through NIL, thereby furnishing mutually complementary two-factor authentication. The resulting three-level hologram suppresses the conjugate image at a specified wavelength (red light) while generating a twin image at other wavelengths, enabling instant visual verification of authenticity. In parallel, a fiducial mark engraved on each film designates the region to be examined with a portable microscope; the quantitatively readable nanopattern is converted into a unique security code, delivering a robust secondary verification.

However, several technical challenges still persist. Precise control of the etch rate has yet to be achieved, and volumetric shrinkage during UV curing introduces deviations between the designed and realized cascade heights. Although only three discrete height levels were demonstrated, extending the cascade architecture to a greater number of levels will necessitate further process optimization, including rigorous etch-rate characterization under diverse conditions and predictive simulations of volume shrinkage. Moreover, because the current design does not explicitly account for the angle of incidence, the hologram image can vary with illumination angle (Figure S16 and Figure S17). This limitation could be mitigated by further refining the cascade architecture, for example through an increased number of relief levels with optimized spacing, together with angular-tolerant CGH optimization.

Finally, translating the proposed platform into practical security devices will require integration with scalable manufacturing strategies. Recent advances in metasurface fabrication have progressed from wafer-scale NIL toward roll-to-roll processing, which could be adapted to the present cascade-nanostructure imprinting process for continuous, high-throughput production.[41] Moreover, emerging multifunctional and switchable metasurface architectures provide additional degrees of freedom in wavefront manipulation, enabling advanced functions such as multichannel information processing, dynamic optical modulation, and system-level integration.[42−45] In this context, the nanostructured film and deposited Ag layer may potentially be exploited as a surface-enhanced Raman spectroscopy (SERS)-active interface to read artificially encoded molecular fingerprints, thereby extending the platform toward a third authentication factor and multifunctional sample analysis.[46−48] However, the incorporation of additional analytical modalities would also require suitable readout instruments and calibration protocols, which remain important challenges for practical implementation.

Despite these limitations, the high difficulty of simultaneously replicating both the optical hologram and the nanopattern makes the proposed two-factor authentication platform a substantial advance in anticounterfeiting technology. Successful application to products ranging from electronic devices to high-end consumer goods highlights its broad potential in security and authentication. Future enhancements to the three-level film design could incorporate still more complex encryption functions, further improving security and practicality and positioning the technology as a key element in next-generation protection solutions.

## ■ ASSOCIATED CONTENT

### Supporting Information

The Supporting Information is available free of charge at https://pubs.acs.org/doi/10.1021/acs.nanolett.6c01958.

Experimental methods for three-level reflective DOE design, Si master mold fabrication, polymer mold replication, Ag deposition, optical microscope image processing, cascaded Fresnel transform model, CD-dependent phase averaging and phasor analysis, comparison of binary- and three-level DOE reconstructions, fabrication process flow, etch-depth uniformity, fabrication-tolerance simulation, NIL film-to-film reproducibility, wavelength-dependent hologram and RGB-channel analyses, practical durability tests, security-code image-processing workflow, film-to-film parameter distribution, repeatability under focus and illumination variations,

Downloaded from pubs.acs.org/nalefd/article-pdf/26/30/9836/6514034/acs.nanolett.6c01958.pdf by KOREA UNIV user on 14 August 2026



https://doi.org/10.1021/acs.nanolett.6c01958
Nano Lett. 2026, 26, 9836−9846

oblique-incidence simulation, and angular tolerance analysis (PDF)

## AUTHOR INFORMATION


### Corresponding Authors

**Hwi Kim** − *Department of Electronics and Information Engineering, Korea University, Sejong 30019, Republic of Korea;* orcid.org/0000-0002-4283-8982; Email: hwikim@korea.ac.kr

**Junseong Ahn** − *Department of Control and Instrumentation Engineering, Korea University, Sejong 30019, Republic of Korea;* orcid.org/0000-0002-4090-5440; Email: junseong@korea.ac.kr

**Jun-Ho Jeong** − *Nano Lithography and Manufacturing Research Center, Korea Institute of Machinery and Materials (KIMM), Daejeon 34103, Republic of Korea; College of Medicine, Chung-Ang University, Seoul 06974, Republic of Korea;* orcid.org/0000-0003-0671-0225; Email: jhjeong@kimm.re.kr

### Authors

**Jinhyeok Yang** − *Department of Control and Instrumentation Engineering, Korea University, Sejong 30019, Republic of Korea;* orcid.org/0009-0004-6473-4115

**Myeonggyu Choi** − *Department of Electronics and Information Engineering, Korea University, Sejong 30019, Republic of Korea*

**Ji-Hwan Ha** − *Department of Mechanical Engineering, Hanbat National University, Daejeon 34158, Republic of Korea*

**Jihyeon Ahn** − *Department of Mechanical Engineering, Korea Advanced Institute of Science and Technology (KAIST), Daejeon 34141, Republic of Korea; Nano Lithography and Manufacturing Research Center, Korea Institute of Machinery and Materials (KIMM), Daejeon 34103, Republic of Korea*

**Soon Hyoung Hwang** − *Nano Lithography and Manufacturing Research Center, Korea Institute of Machinery and Materials (KIMM), Daejeon 34103, Republic of Korea*

**Sohee Jeon** − *Nano Lithography and Manufacturing Research Center, Korea Institute of Machinery and Materials (KIMM), Daejeon 34103, Republic of Korea; College of Pharmacy, Chung-Ang University, Seoul 06974, Republic of Korea*

**Dabin Kim** − *Department of Control and Instrumentation Engineering, Korea University, Sejong 30019, Republic of Korea*

**Jaehoon Jeong** − *Department of Control and Instrumentation Engineering, Korea University, Sejong 30019, Republic of Korea*

**Minki Kim** − *Department of Control and Instrumentation Engineering, Korea University, Sejong 30019, Republic of Korea*

**Hakhyun Lim** − *Department of Control and Instrumentation Engineering, Korea University, Sejong 30019, Republic of Korea*

**Byung-Ho Kang** − *Department of Mechanical Engineering, Korea Advanced Institute of Science and Technology (KAIST), Daejeon 34141, Republic of Korea; Nano Lithography and Manufacturing Research Center, Korea Institute of Machinery and Materials (KIMM), Daejeon 34103, Republic of Korea*

**Jong-An Choi** − *Department of Mechanical Engineering, Korea Advanced Institute of Science and Technology (KAIST), Daejeon 34141, Republic of Korea; Nano Lithography and Manufacturing Research Center, Korea Institute of Machinery and Materials (KIMM), Daejeon 34103, Republic of Korea;* orcid.org/0009-0002-4125-1714

**Byeongmin Kang** − *Department of Mechanical Engineering, Korea Advanced Institute of Science and Technology (KAIST), Daejeon 34141, Republic of Korea; Nano Lithography and Manufacturing Research Center, Korea Institute of Machinery and Materials (KIMM), Daejeon 34103, Republic of Korea*

Complete contact information is available at: https://pubs.acs.org/10.1021/acs.nanolett.6c01958


### Author Contributions

J.Y. and M.C. contributed equally to this work. H.K., Junseong A., and J.-H.J. supervised the work. M.C. performed the computer-generated holography design and optical simulations. J.Y. fabricated the cascade-nanostructured hologram films, conducted structural and optical characterizations, and performed the two-factor authentication demonstrations. J.-H.H. assisted with nanoimprint process optimization. Jihyeon A. assisted with Si master mold fabrication. S.H.H. assisted with nanolithography process development. S.J. assisted with Ag deposition and film replication. D.K. assisted with optical measurements. J.J. assisted with microscope-image processing and security-code analysis. M.K. assisted with durability tests. H.L. assisted with device demonstration and data visualization. B.-H.K. assisted with SEM/FIB characterization. J.-A.C. assisted with structural analysis. B.K. assisted with fabrication process optimization. All authors discussed the results, commented on the manuscript, and have given approval to the final version of the manuscript.

### Notes

The authors declare no competing financial interest.

## ACKNOWLEDGMENTS

This work was supported by Alchemist Project grant funded by Korea Evaluation Institute of Industrial Technology (KEIT) & the Korea Government (MOTIE) (Project Number: 1415179744, 20019169), the Ministry of Culture, Sports and Tourism and Korea Creative Content Agency (Project Number: RS-2024-00343692), the Basic Research Program of KIMM (Korea Institute of Machinery and Materials, NK255D), the National Research Foundation of Korea (NRF) grant funded by the Korean government (MSIT) (Project Number: RS-2024-00358092, RS-2025-00523026), the Korea Evaluation Institute of Industrial Technology (KEIT) grant funded by the Korea government (MOTIE) (Project Number: RS-2022-00154781, Development of large-area wafer-level flexible/stretchable hybrid sensor platform technology for form-factor-free highly integrated convergence sensor), and a Korea University Grant.

## REFERENCES

(1) Sundararajan, S.; Darney, P. E.; Rajan, K. P.; Fernando, A. V.; Jothi, J. N.; Krishnan, R. S. An AI-Enhanced IoT Model for Three-Way Authentication and Location Tracking in Secured Jewellery Boxes. *2024 5th International Conference on Mobile Computing and Sustainable Informatics (ICMCSI)*. IEEE: 2024; pp 755−960.

(2) Syed, W. K.; Mohammed, A.; Reddy, J. K.; Dhanasekaran, S. Biometric Authentication Systems in Banking: A Technical Evaluation of Security Measures. *2024 IEEE 3rd World Conference on Applied Intelligence and Computing (AIC)*. IEEE: 2024; pp 1331−1336.

(3) Rassay, S.; Ramezani, M.; Shomaji, S.; Bhunia, S.; Tabrizian, R. Clandestine Nanoelectromechanical Tags for Identification and Authentication. *Microsystems & Nanoengineering* **2020**, *6*, 103.

Downloaded from pubs.acs.org/naleld/article-pdf/26/30/9836/6514034/acs.nanolett.6c01958.pdf by KOREA UNIV user on 14 August 2026

(4) Lin, R.; Kim, H. J.; Achavananthadith, S.; Kurt, S. A.; Tan, S. C. C.; Yao, H.; Tee, B. C. K.; Lee, J. K. W.; Ho, J. S. Wireless Battery-Free Body Sensor Networks Using near-Field-Enabled Clothing. *Nat. Commun.* **2020**, *11*, 444.
(5) Li, J.; Crown, A.; Ney, P.; Yekhanin, S.; Partap, A.; Shirole, A.; Jiang, H.; Russ, S.; Gordon, M.; Aroh, A.; Nivala, J.; Badam, A.; Ranganathan, V.; Strauss, K.; Chandra, R.; Chen, Y. J. Hybridization-Encoded DNA Tags with Paper-Based Readout for Anti-Forgery Raw Material Tracking. *Nat. Commun.* **2025**, *16*, 5832.
(6) Nanda, A.; Jeong, J. J.; Shah, S. W. A.; Nosouhi, M.; Doss, R. Examining Usable Security Features and User Perceptions of Physical Authentication Devices. *Computers & Security* **2024**, *139*, 103664.
(7) Kim, S.; Lim, J.; Kim, S.; Lee, J. Near-Infrared Luminescent Imaging-Based 3D QR Cube Platform for Spatial Information Storage and Security. *Adv. Mater.* **2025**, *37*, 2416121.
(8) Raval, K. J.; Jadav, N. K.; Rathod, T.; Tanwar, S.; Vimal, V.; Yamsani, N. A Survey on Safeguarding Critical Infrastructures: Attacks, AI Security, and Future Directions. *International Journal of Critical Infrastructure Protection* **2024**, *44*, 100647.
(9) Gadotti, A.; Rocher, L.; Houssiau, F.; Creţu, A.-M.; De Montjoye, Y.-A. Anonymization: The Imperfect Science of Using Data While Preserving Privacy. *Science advances* **2024**, *10*, No. eadn7053.
(10) Awaysheh, F. M.; Aladwan, M. N.; Alazab, M.; Alawadi, S.; Cabaleiro, J. C.; Pena, T. F. Security by Design for Big Data Frameworks Over Cloud Computing. *IEEE Transactions on Engineering Management* **2022**, *69*, 3676−3693.
(11) Kim, G.; Kim, D.; Lee, J. H.; Kim, J.; Heo, S. Y.; Song, Y. M.; Jeong, H. H. Quasi-Ordered Plasmonic Metasurfaces with Unclonable Stochastic Scattering for Secure Authentication. *Nat. Commun.* **2025**, *16*, 6269.
(12) Liu, Y.; Han, F.; Li, F.; Zhao, Y.; Chen, M.; Xu, Z.; Zheng, X.; Hu, H.; Yao, J.; Guo, T.; Lin, W.; Zheng, Y.; You, B.; Liu, P.; Li, Y.; Qian, L. Inkjet-Printed Unclonable Quantum Dot Fluorescent Anti-Counterfeiting Labels with Artificial Intelligence Authentication. *Nat. Commun.* **2019**, *10*, 2409.
(13) Panaitescu, D. M.; Oprică, G. M.; Gabor, A. R.; Nicolae, C. A.; Frone, A. N.; Mihăilescu, M. Proposal of a Biobased and Biodegradable Polymer as a Hot Embossing Substrate for Holographic Security Marks Fabrication. *Polym. Adv. Technol.* **2024**, *35*, No. e6626.
(14) Tomar, A.; Gupta, R. R.; Mehta, S. K.; Sharma, S. An Overview of Security Materials in Banknotes and Analytical Techniques in Detecting Counterfeits. *Critical Reviews in Analytical Chemistry* **2024**, *54*, 2865−2878.
(15) Sun, H.; Maji, S.; Chandrakasan, A. P.; Marelli, B. Integrating Biopolymer Design with Physical Unclonable Functions for Anti-counterfeiting and Product Traceability in Agriculture. *Science Advances* **2023**, *9*, No. eadf1978.
(16) Gu, Y.; He, C.; Zhang, Y.; Lin, L.; Thackray, B. D.; Ye, J. Gap-Enhanced Raman Tags for Physically Unclonable Anticounterfeiting Labels. *Nat. Commun.* **2020**, *11*, 516.
(17) Kim, J. H.; Jeon, S.; In, J. H.; Nam, S.; Jin, H. M.; Han, K. H.; Yang, G. G.; Choi, H. J.; Kim, K. M.; Shin, J.; Son, S. W.; Kwon, S. J.; Kim, B. H.; Kim, S. O. Nanoscale Physical Unclonable Function Labels Based on Block Co-Polymer Self-Assembly. *Nature Electronics* **2022**, *5*, 433−442.
(18) Goncharsky, A.; Goncharsky, A.; Melnik, D.; Durlevich, S. Nanooptical Elements for Visual Verification. *Sci. Rep.* **2021**, *11*, 2426.
(19) Goncharsky, A.; Goncharsky, A.; Durlevich, S. Diffractive Optical Element for Creating Visual 3D Images. *Opt. Express* **2016**, *24*, 9140−9148.
(20) Yao, M.; Wei, W.; Qiao, W.; Zhang, Y.; Zhou, X.; Li, Z.; Peng, H.; Xie, X. High-Security Plastic with Integrated Holographic and Phosphorescent Images. *Adv. Mater.* **2025**, *37*, 2414894.
(21) Rößler, F.; Kunze, T.; Lasagni, A. F. Fabrication of Diffraction Based Security Elements Using Direct Laser Interference Patterning. *Opt. Express* **2017**, *25*, 22959−22970.
(22) Fang, Q.; Liu, J.; Yan, Z.; Deng, Q.; Pang, H.; Lv, Y.; Sun, X.; Chen, J.; Jiang, H.; Yin, S. Liquid-Crystal-Polymer Binary Diffractive Optical Elements with a Sub-Micrometer Feature Size Realized by a Contact Polarization Holography. *Opt. Lett.* **2022**, *47*, 3195−3198.
(23) Wlodarczyk, K. L.; Ardron, M.; Weston, N. J.; Hand, D. P. Holographic Watermarks and Steganographic Markings for Combating the Counterfeiting Practices of High-Value Metal Products. *Journal of Materials Processing Technology* **2019**, *264*, 328−335.
(24) Kazanskiy, N. L.; Khonina, S. N.; Butt, M. A. Exploring the Functional Characteristics of Diffractive Optical Element: A Comprehensive Review. *Optics & Laser Technology* **2025**, *183*, 112383.
(25) You, R.; Hong, Z.; Chen, J.; Zhang, Z.; Wang, Y.; Sun, Y.; Song, B.; Loy, D. A.; Ji, Z.; Liang, R. Extremely Compact 3D Printed Glass Ternary Diffractive Optical Element for Holographic Images. *Advanced Optical Materials* **2025**, *13*, 2501074.
(26) Shen, C. Y.; Batoni, P.; Yang, X.; Li, J.; Liao, K.; Stack, J.; Gardner, J.; Welch, K.; Ozcan, A. Broadband Unidirectional Visible Imaging Using Wafer-Scale Nano-Fabrication of Multi-Layer Diffractive Optical Processors. *Light: Science & Applications* **2025**, *14*, 267.
(27) Dorrah, A. H.; Park, J. S.; Palmieri, A.; Capasso, F. Free-Standing Bilayer Metasurfaces in the Visible. *Nat. Commun.* **2025**, *16*, 3126.
(28) Khonina, S. N.; Kazanskiy, N. L.; Skidanov, R. V.; Butt, M. A. Advancements and Applications of Diffractive Optical Elements in Contemporary Optics: A Comprehensive Overview. *Advanced Materials Technologies.* **2025**, *10*, 2401028.
(29) Okui, M.; Wakunami, K.; Oi, R.; Ichihashi, Y.; Jackin, B. J.; Yamamoto, K. Copying of Holograms by Spot Scanning Approach. *Appl. Opt.* **2018**, *57*, 4117−4122.
(30) Hedlund, C.; Blom, H.-O.; Berg, S. Microloading Effect in Reactive Ion Etching. *Journal of Vacuum Science & Technology A: Vacuum, Surfaces, and Films* **1994**, *12*, 1962−1965.
(31) Yeom, J.; Wu, Y.; Selby, J. C.; Shannon, M. A. Maximum Achievable Aspect Ratio in Deep Reactive Ion Etching of Silicon Due to Aspect Ratio Dependent Transport and the Microloading Effect. *Journal of Vacuum Science & Technology B: Microelectronics and Nanometer Structures Processing, Measurement, and Phenomena* **2005**, *23*, 2319−2329.
(32) Im, D.; Moon, E.; Park, Y.; Lee, D.; Hahn, J.; Kim, H. Phase-Regularized Polygon Computer-Generated Holograms. *Opt. Lett.* **2014**, *39*, 3642−3645.
(33) Li, M.; Chen, Y.; Luo, W.; Cheng, X. Interfacial Interactions during Demolding in Nanoimprint Lithography. *Micromachines* **2021**, *12*, 349.
(34) Johnson, S.; Burns, R.; Kim, E. K.; Dickey, M.; Schmid, G.; Meiring, J.; Burns, S.; Willson, C. G.; Convey, D.; Wei, Y.; Fejes, P.; Gehoski, K.; Mancini, D.; Nordquist, K.; Dauksher, W. J.; Resnick, D. J. Effects of Etch Barrier Densification on Step and Flash Imprint Lithography. *J. Vac. Sci. Technol. B* **2005**, *23*, 2553−2556.
(35) Shibata, M.; Horiba, A.; Nagaoka, Y.; Kawata, H.; Yasuda, M.; Hirai, Y. Process-Simulation System for UV-Nanoimprint Lithography. *J. Vac. Sci. Technol. B* **2010**, *28*, C6M108−C6M113.
(36) Tochino, T.; Shiotsu, T.; Uemura, K.; Yasuda, M.; Kawata, H.; Hirai, Y. Impact of Resist Shrinkage on the Template Release Process in Nanoimprint Lithography. *J. Vac. Sci. Technol. B* **2014**, *32*, 06FG08.
(37) Amirsadeghi, A.; Lee, J. J.; Park, S. Polymerization Shrinkage Stress Measurement for a UV-Curable Resist in Nanoimprint Lithography. *Journal of Micromechanics and Microengineering* **2011**, *21*, 115013.
(38) Zhao, C.-Z.; Cai, Y.-J.; Sun, Y.-X.; Wu, Y.-G.; Sang, K.-X.; Yue, T.; Yang, Z.-H.; Gai, J.-G. Low Volume Shrinkage, Alkaline Degradable UV Nanoimprint Lithography Resists Based on Acrylic Anhydride. *Nanoscale* **2025**, *17*, 1013−1020.
(39) Liu, Z.; Liu, Q.; Ren, X.; Xie, J.; Chang, N.; Zhang, Q. Novel Photobase Generators Mediated Thiol-Epoxy "Click" Reaction for Self-Healing, Degradable and Recyclable Photoresist Based on Bio-Vanillin and Eugenol. *Chemical Engineering Journal* **2025**, *503*, 158304.
(40) Lim, H.; Choi, J.; Han, C.; Kim, D.; Jin, H.; Kim, M.; Kim, Y.; Yang, J.; Seo, S.; Jung, J.; Ju, H.; Hong, C.-H.; Lee, D.; Ahn, J.; Kim, H. J. Scalable In-Situ Fabrication of Multimodal Electronic Skin for Intelligent Robotics and Interactive Systems. *npj Flexible Electronics* **2026**, *10*, 34.

Downloaded from pubs.acs.org/naleif/article-pdf/26/30/9836/6514034/acs.nanolett.6c01958.pdf by KOREA UNIV user on 14 August 2026


https://doi.org/10.1021/acs.nanolett.6c01958
*Nano Lett.* 2026, 26, 9836−9846

(41) Hoang, T.; Park, Y.; Kim, J.; Truong, H.; Parajuli, S.; Rajasekaran, B. J.; Kim, K.; Kang, D.; Jeon, G.; Lee, K.-i.; Yoon, D. H.; Kim, I.; Rho, J.; Cho, G. 300-Unit-per-Second Roll-to-Roll Manufacturing of Visible Metalenses. *Nature* **2026**, *652*, 1188−1194.
(42) Moon, S.; Kim, J.; Jo, Y.; Seo, J.; Kim, K.; Kim, S.; Lee, C.-K.; Rho, J. Switchable 2D-3D Display through a Metasurface Lenticular Lens. *Nature* **2026**, *652*, 1181−1187.
(43) Oh, D. K.; Kang, H.; Kang, D.; Kim, J.; Rho, J. Nanoprinting Metasurfaces with Engineered Optical Materials. *Nature Reviews Materials* **2026**, *11*, 375−392.
(44) Kim, Y.; Lee, J.; Kim, W.-S.; Heo, H.; Jeon, D.; Yang, B.; Li, X.; Keawmuang, H.; Hu, S.; Kim, Y.-K.; Badloe, T.; Rho, J. Millisecond-Level Electrically Switchable Metalens for Adaptive Rotational Depth Mapping and Diffraction-Limited Imaging. *Opto-Electronic Advances* **2026**, *9*, 250216.
(45) Jia, T.; Jeon, Y.; Feng, L.; Kim, H.; Li, B.; Rui, G.; Rho, J. Superchirality Induced Ultrasensitive Chiral Detection in High-Q Optical Cavities. *Opto-Electronic Advances* **2025**, *8*, 250079.
(46) Ha, J. H.; Yang, J.; Kim, D.; Lee, W.; Yun, C.; Hwang, S. H.; Jeon, S.; Choi, J.; Lim, H.; Kim, M.; Kim, D.; Park, S. A.; Choi, J.; Song, J. W.; So, S.; Ahn, J.; Jeong, J. H. SERS Sensor Integrated in Stretchable and Antimicrobial Wrapper for Food Quality Monitoring and Preservation. *Small* **2025**, *21*, 2501808.
(47) Zhao, Z. J.; Ahn, J.; Hwang, S. H.; Ko, J.; Jeong, Y.; Bok, M.; Kang, H. J.; Choi, J.; Jeon, S.; Park, I.; Jeong, J. H. Large-Area Nanogap-Controlled 3D Nanoarchitectures Fabricated via Layer-by-Layer Nanoimprint. *ACS Nano* **2021**, *15*, 503−514.
(48) Zhao, Z. J.; Ahn, J.; Ko, J.; Jeong, Y.; Bok, M.; Hwang, S. H.; Kang, H. J.; Jeon, S.; Choi, J.; Park, I.; Jeong, J. H. Shape-Controlled and Well-Arrayed Heterogeneous Nanostructures via Melting Point Modulation at the Nanoscale. *ACS Appl. Mater. Interfaces* **2021**, *13*, 3358−3368.

Downloaded from pubs.acs.org/nalefd/article-pdf/26/30/9836/6514034/acs.nanolett.6c01958.pdf by KOREA UNIV user on 14 August 2026



https://doi.org/10.1021/acs.nanolett.6c01958
*Nano Lett.* 2026, 26, 9836−9846